Modelling the Bioelectronic Interface in Engineered Tethered Membranes: From Biosensing to Electroporation

William Hoiles, Vikram Krishnamurthy, *Fellow, IEEE*, and Bruce Cornell

***Abstract*—This paper studies the construction and predictive models of three novel measurement platforms: (i) a Pore Formation Measurement Platform (PFMP) for detecting the presence of pore forming proteins and peptides, (ii) the Ion Channel Switch (ICS) biosensor for detecting the presence of analyte molecules in a fluid chamber, and (iii) an Electroporation Measurement Platform (EMP) that provides reliable measurements of the electroporation phenomenon. Common to all three measurement platforms is that they are comprised of an engineered tethered membrane that is formed via a rapid solvent exchange technique allowing the platform to have a lifetime of several months. The membrane is tethered to a gold electrode bioelectronic interface that includes an ionic reservoir separating the membrane and gold surface, allowing the membrane to mimic the physiological response of natural cell membranes. The electrical response of the PFMP, ICS, and EMP are predicted using continuum theories for electrodiffusive flow coupled with boundary conditions for modelling chemical reactions and electrical double layers present at the bioelectronic interface. Experimental measurements are used to validate the predictive accuracy of the dynamic models. These include using the PFMP for measuring the pore formation dynamics of the antimicrobial peptide PGLa and the protein toxin Staphylococcal α-Hemolysin; the ICS biosensor for measuring nano-molar concentrations of streptavidin, ferritin, thyroid stimulating hormone (TSH), and human chorionic gonadotropin (pregnancy hormone hCG); and the EMP for measuring electroporation of membranes with different tethering densities, and membrane compositions.**

***Index Terms*—Bioelectronic interface, biosensing, chemical reaction kinetics, electroporation, generalized Poisson–Nernst–Planck, tethered bilayer lipid membrane.**

I. Introduction

A fundamental difference between the recognition, sensing, and signalling technologies developed by the bioelectronics industry, and that which occurs in nature, is that the charge carrier in biological systems is an ion rather than an electron. A number of differences result from this including:

1) the diffuse three dimensional distribution of ions in solution relative to the well-defined localisation of electrons in metals;
2) the slow kinetics of ions in solution compared to the relatively instantaneous kinetics of electrons in metals.

These effects have been recruited by nature to be the controlling phenomenon in the time dependent currents in cellular action potentials, in the propagation of action potentials along nerve fibres, and in the transduction mechanisms of the many sensory functions found in sentient life.

The bioelectronic interface is the physical barrier that must be understood and controlled to permit communication between the complex ephemeral systems of biology and the far faster, better defined, and more robust inorganic world of electronics. An increasingly powerful tool in achieving this understanding is the tethered membrane which incorporates components of real cell membranes. The tethered membrane is designed to mimic the physiological response of real cell membranes.

In this paper the novel engineering and predictive models of 3 related measurement platforms, namely the Pore Formation Measurement Platform (PFMP), Ion Channel Switch (ICS) biosensor, and the Electroporation Measurement Platform (EMP) are presented. The three measurement platforms employ an engineered tethered membrane that mimics the electrophysiological properties of real cell membranes, and a gold electrode bioelectronic interface to which electrical instrumentation is connected. Common to all three platforms is that the measurements are performed by estimating the time-dependent conductance of the engineered tethered membrane which is dependent on the bioelectronic interface, and the ensemble of aqueous pores and conducting ion-channels present.

The use of inert gold electrodes as the bioelectronic interface is superior to redox active electrodes for two reasons. First, if redox active electrodes are used, the metal will ablate causing the tethers to dissociate from the electrode surface destroying the membrane [1]. Second, redox active electrodes release metal ions into solution which can interfere with the electrophysiological response of proteins and peptides. The inert gold electrode capacitively couples the electronic domain to the physiological domain without the issues associated with redox electrodes, however the capacitive effects of the electrode must be accounted for when modelling the three measurement platforms.

A schematic of the engineered tethered membrane is given in Fig. 1. Key features of the engineered tethered membrane are that the experimentalist can select the density of tethers and membrane composition with the constructed membrane having a lifetime of several months [1]–[6]. The engineered tethered

Manuscript received March 27, 2014; revised July 17, 2014; accepted September 03, 2014. Date of publication October 31, 2014; date of current version May 22, 2015. This paper was recommended by Associate Editor R. Butera.

W. Hoiles and V. Krishnamurthy are with the Department of Electrical and Computer Engineering, University of British Columbia, Vancouver, BC V6T 1Z4, Canada (e-mail: whoiles@ece.ubc.ca; vikramk@ece.ubc.ca).

B. Cornell is with Surgical Diagnostics Ltd., Roseville, Sydney 2069, Australia (e-mail: surgicaldiagnostics.com).

Digital Object Identifier 10.1109/TBCAS.2014.2357420

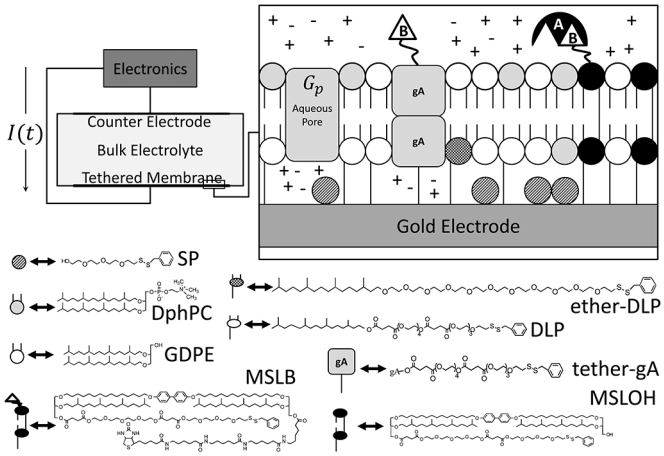

Fig. 1. Overview of the engineered tethered membrane and molecular components. The "Electronics" block represents the electronic instrumentation that produces the drive potential between the electrode and counter electrode, and records the current response $I(t)$. G_p is an aqueous pore that is governed by electroporation. The conducting gA dimer is shown and is composed of two gA monomers. A represents the analyte species, and B the analyte receptor.

membrane is composed of a self-assembled monolayer of mobile lipids, and a self-assembled monolayer of tethered and mobile lipids. The tethered lipids are anchored to the gold electrode via polyethylene glycol chains. Spacer molecules are used to ensure the tethers are spread over the gold electrode. The intrinsic spacing between tethers and spacers is maintained by the benzyl disulphide moieties. A time-dependent voltage potential is applied between the electrodes to induce a transmembrane potential of electrophysiological interest; this results in a current $I(t)$ that is dependent on the charging of the electrical double-layers and the conductance of the engineered tethered membrane.

In the rest of this introductory section, we explain the context and related literature for each of the three measurement platforms, and finally discuss the similarities of these platforms in terms of construction, the dynamics of membrane conductance, and modelling.

1) Pore Formation Measurement Platform: The PFMP is used to detect the presence of pore forming proteins and peptides. Since the membrane surface is engineered to mimic prokaryotic, eukaryotic, and archaebacterial membranes, the PFMP can be used to measure the specificity of attack of protein and peptide toxins. Therefore, the PFMP can be used for rapid point-of-care detection of pore forming toxins and for inexpensive pharmacology screening of novel antimicrobial peptides. Examples of tethered bilayer lipid membranes for the measurement of pore forming toxins include [7] in which the membrane is composed of diphytanyl chains that are coupled via a glycerol to oligoethylene oxide spacers, and [8] that uses different lipid, anchoring, and spacer components then the PFMP but employs an identical solvent-exchange membrane formation protocol. Pore forming protein toxins are the most potent biological weapons in nature and are key to the attack mechanism of *Methicillin-resistant Staphylococcus aureus* (MRSA), commonly known as the "super bug" bacteria. Rapid detection of pore-forming protein toxins is vital for effective treatment. Protein toxins diffuse in solution until the protein binds to a specific membrane. The pore forming toxin may oligomerize prior to forming conducting pores in the membrane causing cell lysis and ultimately killing the cell. As the toxin produces conducing pores, measurement of the conductance of the engineered membrane allows the rapid pathogenic detection of such toxins and can be used to isolate which membranes are most susceptible to attack. The construction of the PFMP is given in Section II-A, and the dynamics of the PFMP are modelled using an equivalent circuit model as presented in Section II-B. In Section II-C we apply the PFMP to measure the potency of the antimicrobial peptide PGLa and pore forming toxin α-Hemolysin $(\alpha\mathrm{HL})$, produced by MRSA, against charged and uncharged membranes that mimic the properties of eukaryotic and prokaryotic membranes. As shown, PGLa is suitable for killing bacteria with negatively charged membranes leaving the uncharged membrane intact.

2) Ion Channel Switch Biosensor: The Ion Channel Switch (ICS) biosensor discussed in this paper was originally developed by coauthor Cornell and its construction is detailed in the Nature publication [4]. The ICS biosensor is a fully functioning nanomachine constructed out of a tethered artificial cell membrane with moving parts comprising gramicidin (gA) channels. Gold electrodes constitute the bioelectronic interface between the electrical instrumentation and the electrolyte solution. The ICS biosensor can detect femto-molar concentrations of target species including proteins, hormones, polypeptides, microorganisms, oligonucleotides, DNA segments, and polymers in cluttered electrolyte environments [9]–[11], and has a lifetime of several months [1]–[4], [6]. The ICS biosensor has also been used in clinical trials for the detection of Influenza A [10].

This paper models the dynamics of the ICS biosensor via a distributed system (diffusion partial differential equation) interacting with a lumped circuit (ordinary nonlinear differential equations). Previous models of the ICS have focused on using reaction rate theory [12], and a combination of reaction rate theory and the Nernst-Planck equations for advection-diffusion [9], [11]. The model proposed in this paper has two key advantages to those proposed previously in [9], [11]:

1) the use of surface reaction-diffusion equations to account for the the diffusion kinetics of species on the surface of the membrane;
2) including the equilibrium aqueous pore conductance G_p.

To illustrate the application of the ICS and predictive model for concentration estimation, in Section III-C we compare the predicted membrane conductance with the experimentally measured membrane conductance for four important analyte species: streptavidin, thyroid stimulating hormone (TSH), ferritin, and human chorionic gonadotropin (hCG). The streptavidin to antibody receptor biotin provides an excellent case study for validation of the proposed dynamic model. The concentration of TSH present can be used to detect hypo or hyperthyroidism. Ferritin plays a central role in the transport, storage, and release of iron. It is well known that as the concentration of ferritin increases, this can be directly associated with a pathogenic infection or the presence of cancer. Here we measure the concentration of ferritin in whole blood (i.e., human blood from a standard blood donation). The concentration of hCG is an excellent indicator of the presence of blastocyst or mammalian embryogenesis (i.e., pregnancy).

3) Electroporation Measurement Platform: Electroporation is a phenomenon by which a transmembrane potential applied across a membrane results in the formation of aqueous pores. This allows the passage of otherwise impermeable molecules into a cell such as chemotherapeutic agents, DNA molecules, and neuron specific proteins in drug delivery applications. It is reported in [13] that electroporation can circumvent poor delivery of medications to the central nervous system for Alzheimers, Parkinson's disease, and brain cancer. Though in wide use, the electroporation process is still poorly understood hindering the development of novel electrochemotherapy protocols. The EMP considered in this paper provides a controllable and physiologically relevant environment for the study of electroporation.

To relate the experimentally measured current to the population and dynamics of pore radii requires a dynamic model of electroporation. The most widely used model for the statistics of aqueous pores formed via electroporation is the Smoluchowski-Einstein (SE) equation, which is dependent on the pore energy, derived from statistical mechanics [14]–[16]. Several models governing the pore energy have been presented in the literature [17]–[20]. The membrane is typically modelled as a dielectric and elastic continuum with a pore energy given by [17]–[20]

$$W = 2\pi\gamma r - \pi\sigma r^2 + \left(\frac{C}{r}\right)^4 + W_{\rm es} + 0.5K_{\rm t}r^2 \qquad (1)$$

where γ is the pore edge energy, σ is the membrane surface tension, the electrostatic interaction between lipid heads, the transmembrane potential energy contribution $W_{\rm es}$, and the energy introduced by the tethers $K_{\rm t}$.

In Section IV-A, asymptotic approximations to the Smoluchowski-Einstein and a Generalized Poisson-Nernst-Planck (GPNP) system of equations is used to link the experimentally measured conductance to the population and dynamics of pore radii. The GPNP is equivalent to the Poisson-Nernst-Planck (PNP) system of equations if steric effects are neglected. Recent models for computing pore conductance G_p in the literature use the (PNP), assuming symmetric electrolytes and electroneutrality [21]; and models for computing $W_{\rm es}$ assuming symmetric electrolytes, electroneutrality, and negligible concentration gradients [18]. The evaluation of G_p and $W_{\rm es}$ using the GPNP accounts for the dynamics of electrolytes and the Stern and diffuse layers present in the EMP. Experimental verification of the dynamic model of electroporation in the EMP is presented in Section IV-B for 1%, 10% and 100% tethered membranes for different excitation potentials and membrane compositions.

Unifying Theme: The unifying theme that underpins all 3 measurement platforms is that (a) they all use an inert gold bioelectronic interface, (b) they are constructed using a self-assembled engineered tethered membrane, (c) their dynamics can be modelled using a generalized Poisson-Nernst-Planck system of equations coupled with nonlinear boundary conditions, (d) the sensing mechanism of each relies on measurement of changes in the tethered membrane conductance. Measurement platform 1 (PFMP) detects changes in membrane conductance from pore forming proteins and peptides, measurement platform 2 (ICS) detects changes in membrane conductance as a function of the switching dynamics of gA dimers, and measurement platform 3 (EMP) detects changes in membrane conductance resulting from an elevated transmembrane potential.

The paper proceeds by presenting how each measurement platform is constructed, the predictive models, and then experimental measurements exemplifying the detection capability and model accuracy for each measurement platform. Section II presents the PFMP, Section III the ICS biosensor, and Section IV the EMP. Closing remarks are provided in Section V.

II. Measurement Platform 1: Pore Formation Measurement Platform (PFMP)

In this section the construction, dynamic model, and experimental measurements using the PFMP are presented. The dynamic model and experimental measurements of the PFMP allow the conductance of the tethered membrane to be estimated. Since the membrane conductance is related to the population of conducting pores, detecting changes in the membrane conductance of the PFMP can be related to the pore formation dynamics of peptides and proteins.

A. Pore Formation Measurement Platform: Construction and Formation

The engineered tethered membrane is supported by a $25 \times 75 \times 1$ mm polycarbonate slide. Six 100 nm thick sputtered gold electrodes, each with dimensions 0.7×3 mm, rest on the polycarbonate slide. Each electrode is in an isolated flow cell with a common gold return electrode. The formation of the tethered membrane on the gold electrode is performed in two stages using a solvent-exchange technique.

Stage 1: The first stage of formation involves anchoring of the tethers and spacers to the gold surface. The tethers provide structural integrity to the membrane and mimic the physiological response of the cytoskeletal supports of real cell membranes. The spacers laterally separate the tethers allowing patches of mobile lipids to diffuse in the membrane. The tethers and spacers both contain a benzyl disulphide components (i.e., MSLOH, DLP, ether-DLP, tether-gA, MSLB, and SP in Fig. 1). The sulphur bonded to the benzyl, bonds to the gold surface with the disulphide bond maintained [4], [10]. This bonding structure has been detected experimentally from X-ray photoelectron spectra. The use of the disulphide has the advantage that the thiols do not oxidize on storage allowing the membrane to have a lifetime of several months. From experimental measurements, the electrodesorption of the thiol to gold bond is negligible for electrode potentials below 800 mV [22].

To form the anchoring layer, an ethanolic solution containing 370 μM of engineered ratios of benzyl disulphide components is prepared. The ratio of benzyl disulphide components defines the tethering density of the membrane. For example, for a 10% tethered membrane, for every 9 spacer molecules there is 1 tether molecule. This solution is exposed to the gold surface for 30 min, then the surface is flushed with ethanol and air dried for approximately 2 min. Note that in the special case of 100% tethering, the engineered tethered membrane is composed of a tethered archaebacterial based monolayer with no spacer molecules. As experimentally illustrated in [2], it is not possible to construct

a 0% tethered membrane as any formed membrane binds to the gold surface. As the electrolyte reservoir separating the membrane and electrode surface is required for the normal physiological function of the membrane, and noting that all prokaryotic and eukaryotic cell membranes contain cytoskeletal supports with a 1% to 10% tether density, the inability to construct a 0% tethered membrane is of little importance.

Stage 2: The second stage involves the formation of the tethered membrane. A solution containing a mixture of mobile lipids is brought into contact with the gold bonded components from Stage 1. Several lipid solvents can be used [3], [4], however in most cases the lipids selected to form the bilayer are soluble in ethanol. As an example, let us consider the formation of a 70% DphPC and 30% GDPE mixed tethered membrane. 8 μL of 3 mM of the 70% DphPC and 30% GDPE ethanolic solution is added to the flow chamber. The solution is incubated for 2 min at 20°C in which the tethered membrane forms. Proceeding the 2 min incubation, 300 μL of phosphate buffered saline is flushed through each flow chamber. The tethered membrane is equilibrated for 30 min prior to performing any experimental measurements. The formation of the POPG, E. coli, and S. caerevisae tethered membranes follows a similar procedure and is therefore omitted.

Quality Control and Measurement: The quality of the tethered membrane is measured continuously using an SDx tethered membranes tethaPod swept frequency impedance reader operating at frequencies of 1000, 500, 200, 100, 40, 20, 10, 5, 2, 1, 0.5, 0.1 Hz and an excitation potential of 20 mV (SDx Tethered Membranes, Roseville, Sydney). Custom drive potentials are produced and the resulting current recorded using an eDAQ ER466 potentiostat (eDAQ, Doig, Denistone East) and a SDx tethered membrane tethaPlate adaptor to connect to the assembled electrode and cartridge. The defect density in the formed membrane can be estimated from the impedance measurements using the protocol presented in [23]. For all experimental measurements, the membrane contained negligible defects. To detect the presence of electrodesorption and release of portions of tethered membrane into solution, the capacitance of the gold electrode and membrane is monitored. Using the experimentally measured impedance and dynamic model in Section II-B, the integrity of the sulphur-gold bond and membrane is ensured by comparing the associated capacitances before and after all experimental measurements.

B. Pore Formation Measurement Platform: Dynamic Model

To estimate important biological parameters, such as the membrane capacitance and conductance, from experimental measurements requires a dynamic model. In this section an equivalent circuit model of the tethered membrane platform is constructed that allows the conductance G_m and capacitance C_m of the tethered membrane to be estimated from impedance measurements [2], [5], [24], [25].

The mechanism of pathogenic detection is based on observing membrane conductance changes—that is, if $\delta G_m/\delta t \neq 0$, then conducting pores have formed in the membrane increasing the conduction. Pathogenic toxins form conducting pores via self-association of membrane-bound proteins. Macroscopic current recordings can be used to estimate the time dependent conductance of the membrane G_m. As an ensemble of conducting pores form in the membrane, the macroscopic conductance will very. The change in conductance is a measure of the potency of the pathogenic protein on the membrane. Since the engineered tethered membrane can be designed with different lipids, this allows the classification of pathogenic potency for specific classes of membranes.

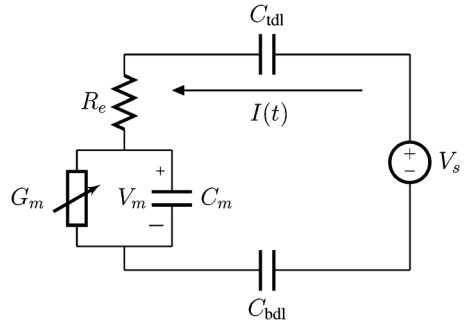

Fig. 2. Schematic of the lumped circuit model for the tethered membrane platform, circuit parameters are defined in Section II-B.

The tethered membrane platform is composed of three distinct regions: the electrical double layers at the gold electrodes, the bulk electrolyte reservoir, and the tethered membrane. The bulk electrolyte solution is modelled as completely ohmic with resistance R_e. The electrical double-layers contain a tightly bound region of ions on the order of an atomic radii, and a diffuse region of length on the order of the Debye-Hückel thickness. The Stern layer and diffuse charge layers are modelled using an overall capacitance C_{tdl}, and C_{bdl} for the counter electrode and electrode respectively. The tethered membrane is modelled as a uniformly polarized structure such that the charging dynamics of the membrane are represented by a capacitance C_m. The tethered membrane conductance, denoted by G_m, models the population of conducting pores in the tethered membrane. The excitation potential $V_s(t)$ applied across the two electrodes closes the circuit. The equivalent circuit model of the tethered membrane platform is given in Fig. 2. The governing equations of the tethered membrane system (Fig. 2) are given by

$$\begin{aligned}\frac{dV_m}{dt} &= -\left(\frac{1}{C_m R_e}+\frac{G_m}{C_m}\right)V_m - \frac{1}{C_m R_e}V_{dl} + \frac{1}{C_m R_e}V_s,\\ \frac{dV_{dl}}{dt} &= -\frac{1}{C_{dl} R_e}V_m - \frac{1}{C_{dl} R_e}V_{dl} + \frac{1}{C_{dl} R_e}V_s,\\ I &= \frac{1}{R_e}(V_s - V_m - V_{dl})\end{aligned} \tag{2}$$

where C_{dl} is the total capacitance of C_{tdl} and C_{bdl} in series. The initial conditions of (2) are that $V_m(0) = 0$ and $V_{dl}(0) = 0$. Given $V_s(t)$, and the static circuit parameters C_{tdl}, C_{bdl}, R_e, and C_m, the membrane conductance G_m can be estimated from the measured current $I(t)$.

C. Pore Formation Measurement Platform: PGLa, α-Hemolysin Experimental Results

In this section the pore formation dynamics of the antimicrobial peptide PGLa, and the pore forming toxin αHL are studied using experimental measurements and dynamic model of the

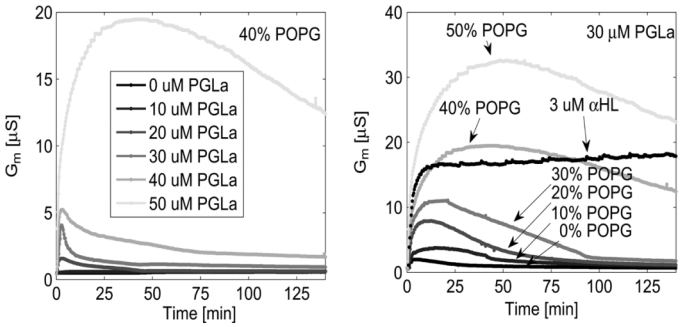

Fig. 3. Experimentally measured tethered membrane conductance resulting from PGLa and Staphylococcal α-Hemolysin interaction with charged and uncharged tethered membranes. The experimental data in this figure is obtained from [1].

PFMP presented in Section II-B. Recall that the population of conducting pores in the membrane can be estimated given the membrane conductance G_m. A tether density of 10% is selected to mimic the cytoskeletal supports of real cells, and uncharged DphPC, and charged 0–50% POPG tethered membranes are utilized to estimate the potency of PGLa and αHL on prokaryotic and eukaryotic membranes.

Fig. 3 presents the estimated tethered membrane conductance G_m from the experimentally measured impedance and dynamic model (2) for the response of uncharged and charged tethered membranes in contact with PGLa and αHL. As expected, as the percentage of negatively charged lipids (i.e., POPG) increases, an increase in the population of PGLa pores results. Comparing the conductance dynamics from PGLa and αHL in contact with the uncharged membrane, it is clear that αHL is significantly more potent then PGLa. This is expected as αHL is a protein toxin that preferentially attacks uncharged eukaryotic membranes, whereas PGLa attacks negatively charged prokaryotic bacterial membranes. Fig. 3 shows that as the concentration of PGLa increases and/or the negative charge of the tethered membrane increases the population of PGLa pores increase. Interestingly, unlike αHL, the PGLa pores dissociate on a timescale of 10–60 min even though the concentration of PGLa remains constant. This suggests that the dissociated pores prevent the adsorption and formation of conducting PGLa pores.

III. Measurement Platform 2: Ion Channel-Switch (ICS) Biosensor

In this section the construction, dynamic model, and experimental measurements of the ICS are presented. The ICS biosensor and dynamic model allow the concentration of important biological analytes in cluttered electrolyte environments to be estimated. To validate the dynamic model, experimental measurements of streptavidin and ferritin are provided.

A. Ion Channel-Switch Biosensor: Formation

The formation of the ICS biosensor is described in Section II-A, with the ethanol solution in Stage 2 containing biotinylated gA monomers (tether-gA in Fig. 1) with the biotin linked to the gA monomer via a 5-aminocaproyl linker. For the detection of streptavidin the antibody biotin is used. The associated antibody fragments used to detect ferritin, TSH, and hCG are the anti-ferritin F'_{ab}, thyrotropin binding inhibitory immunoglobulin, and immunoglobulin G respectively. Details on how the antibodies are connected to the MSLB and mobile gA monomers, in Fig. 1, is provided in [4].

B. Ion Channel-Switch Biosensor: Dynamic Model

In this section a dynamic model is constructed for the ICS biosensor. The dynamic model can be used to estimate the concentration of target analyte species using experimental measurements from the ICS biosensor.

The conductance of the tethered membrane in the ICS biosensor can be estimated from impedance measurements using the circuit model in Fig. 2. G_m is dependent on the population of aqueous pores and conducting gA dimers present. Since a voltage excitation of 20 mV is used, the population of aqueous pores is constant and is accounted for by the associated equilibrium membrane conductance G_o. The total conductance of the of all gA dimers, denoted $G_D(t)$, is proportional to the population of gA dimers present (i.e., $G_D(t) \propto D(t)$ with $D(t)$ the population of gA dimers). To link the membrane conductance G_m to the target analyte concentration requires a model that accounts for the electrodiffusive effects of the analyte in the electrolyte, and the surface reactions present on the tethered membrane surface of the ICS biosensor.

1) Electrodiffusive Model: Classically electrodiffusive dynamics are modelled using the Poisson-Nernst-Planck (PNP) system of equations derived from statistical mechanics assuming all electrolyte ions are point-like [26]. To effectively model the electrical double layers present at the electrode-electrolyte interface and membrane, the steric effects of ions must be accounted for. Using statistical mechanics, the free energy of an electrolyte solution can be estimated with steric effects of ions included using a "Langmuir type" activity coefficient [27]. The chemical potential of the electrolyte is computed by taking the ratio of the change in free energy and change in species concentration. Given the chemical potential of the electrolyte, PDEs governing the electrolyte dynamics can be derived as outlined in [28]. The result of this derivation is the Generalized PNP (GPNP) model given by [29]

$$\begin{aligned}\frac{\partial c^i}{\partial t} &= -\nabla\cdot(J^i) - v\nabla c^i,\\ J^i &= -D^i\nabla c^i - Fz^i q u^i_m c^i\nabla\phi\\ &\quad - D^i c^i \nabla \ln\left(1-\sum_{j=1}^{N} N_{\mathrm{A}} a_j^3 c^j\right), \qquad (3a)\end{aligned}$$

$$\nabla\cdot(\varepsilon\nabla\phi) = -\sum_{i=1}^{N} Fz^i c^i. \qquad (3b)$$

In (3a), J^i is the concentration flux, c^i is the concentration, ϕ is the electrical potential, D^i is the diffusivity, N_{A} is Avagadro's number, a_i is the effective ion size, u^i_m is the ionic mobility with $i \in \{1,2,\ldots,N\}$ denoting the ionic species, and v is the velocity field. In (3b), F is Faraday's constant, q is the elementary charge, z^i is the charge valency of species i, and ε is the electrical permittivity. The electrodiffusive model (3) is able to account for asymmetric electrolytes, multiple ionic species, and the Stern and diffuse electrical double layers

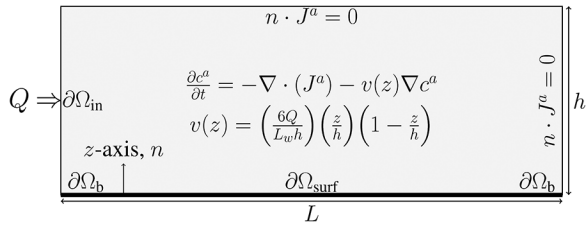

Fig. 4. Schematic of the ICS biosensor model (3a), (4), (5), and (6) with boundary conditions (7). The analyte enters the ICS at $\partial\Omega_{\text{in}}$ with a flow rate of Q. $\partial\Omega_{\text{surf}}$ is the surface of the tethered membrane, and $\partial\Omega_{\text{b}}$ denotes the boundary of the membrane. n denotes the inward normal vector from the surface. Other parameters are defined in Table I.

present at the surface of the electrodes and membrane. Note that for $\sum_{j=1}^{N} N_{\text{A}} a_j^3 c^j \ll 1$, the steric effects are negligible in (3) and the standard PNP formulation can be used to model the electrolyte dynamics.

2) Surface Reactions of ICS Biosensor: The population of dimers $D(t)$ is related to the analyte dynamics (3) by a reaction boundary condition $\partial\Omega_{\text{surf}}$ at the surface of the membrane in contact with the electrolyte. On $\partial\Omega_{\text{surf}}$, analyte molecules bind to the tethered antibody sites followed by a cross-linking of the mobile gA monomers to the bound analytes. The primary species involved in this process include the analytes a, binding sites b, mobile gA monomers c, tethered gA monomers s, and the dimers d, with respective concentrations $\{c^a, c_s^b, c_s^c, c_s^s, c_s^d\}$. Other chemical complexes present include w, x, y, and z with concentrations $\{c_s^w, c_s^x, c_s^y, c_s^z\}$. The chemical reactions that relate these chemical species are described by the following set of reactions [9]–[11]

$$a + b \underset{r_1}{\overset{f_1}{\rightleftharpoons}} w \quad a + c \underset{r_2}{\overset{f_2}{\rightleftharpoons}} x \quad w + c \underset{r_3}{\overset{f_3}{\rightleftharpoons}} y \quad x + b \underset{r_4}{\overset{f_4}{\rightleftharpoons}} y$$
$$c + s \underset{r_5}{\overset{f_5}{\rightleftharpoons}} d \quad a + d \underset{r_6}{\overset{f_6}{\rightleftharpoons}} z \quad x + s \underset{r_7}{\overset{f_7}{\rightleftharpoons}} z. \tag{4}$$

In (4), r_i and f_i, for $i \in \{1,2,3,4,5,6,7\}$, denote the reverse and forward reaction rates for the chemical species $\{a, b, c, d, s, w, x, y, z\}$. An explanation of the reactions that take place can be found in [11]. The dynamics of the surface bound species are modelled using a set of surface reaction-diffusion equations given by

$$\frac{\partial c_s^j}{\partial t} = \nabla_s \cdot \left(D_s^i \nabla_s c^j\right) + R_s^j. \tag{5}$$

In (5), c_s^j is the surface concentration of species $j \in \{a, b, c, d, w, x, y, z\}$, D_s^i is the surface diffusion, R_s^j is the change in concentration resulting from chemical reactions, and ∇_s is the surface gradient.

Given the time-scale of the conductance measurements is seconds, we assume that the velocity field v is a fully developed laminar flow with a parabolic velocity profile given by

$$v(z) = \left(\frac{6Q}{L_w h}\right)\left(\frac{z}{h}\right)\left(1 - \frac{z}{h}\right) \tag{6}$$

where Q, W, and h are defined in Fig. 4 and Table I.

For typical uncharged analyte species we set $z^i = 0$ and $a_i = 0$ in (3) which reduces the system of non-linear PDEs in (3) into the standard advection-diffusion PDE (3a). The boundary and initial conditions of (3a) and (5) are given by

$$n \cdot D^a \nabla c^a = R_s^a \text{ in } \partial\Omega_{\text{surf}}, \quad n \cdot D^a \nabla c^a = 0 \text{ otherwise},$$
$$c^a = c_o^a \text{ in } \partial\Omega_{\text{in}}, \quad n \cdot D_s^j \nabla_s c_s^j = 0 \text{ in } \partial\Omega_{\text{b}} \tag{7}$$

with $\partial\Omega_{\text{surf}}$, $\partial\Omega_{\text{in}}$, and $\partial\Omega_{\text{b}}$ defined in Fig. 4, and intial conditions $c^a(0) = 0$ and $c_s^j(0)$ defined in Table I. In (7), R_s^a couples the change in analyte concentration (units of mol/m^3) to the change in surface bound species concentration (units of mol/m^2) via (4), and c_o^a is the input analyte concentration.

The surface concentration of gA dimers, denoted by c_s^d, is computed from (3a), (4), (5), and (6) with the boundary conditions (7), and is related to the membrane conductance by

$$\hat{G}_m(t) = \kappa \int_{\partial\Omega_{\text{surf}}} c_s^d(t) dS + G_o \tag{8}$$

where $\hat{G}_m(t)$ is the estimated conductance, κ is the proportionality constant relating the conductance of the gA dimers to the number of gA dimers, with $\partial\Omega_{\text{surf}}$ defined in Fig. 4.

TABLE I
MODEL PARAMETERS FOR ICS BIOSENSOR

Symbol	Definition	Value
c_o^A	inlet analyte concentration	100 fM-353 nM
$c_s^c(0)$	mobile gA monomers	16-33 pmol/m^2
$c_s^b(0)$	tethered binding sites	16-166 pmol/m^2
$c_s^d(0)$	gA dimers	16-33 pmol/m^2
$c_s^s(0)$	tethered gA monomers	16-33 pmol/m^2
$c_s^w(0), c_s^x(0), c_s^y(0), c_s^z(0)$	initial surface concentration	0 mol/m^2
$f_1 = f_2 = f_6$	forward reaction rate	5×10^2–8×10^3 m^3/smol
$f_3 = f_4$	forward reaction rate	3×10^9–3×10^{11} m^2/smol
$f_5 = f_7$	forward reaction rate	6×10^8–3×10^{11} m^2/smol
$r_1 = r_2 = r_6$	reverse reaction rate	$10^{-6} - 10^{-4}$ s^{-1}
$r_3 = r_4$	reverse reaction rate	$10^{-6} - 10^{-4}$ s^{-1}
$r_5 = r_7$	reverse reaction rate	1×10^{-4}–1.5×10^{-2} s^{-1}
D^a	Diffusivity of analyte A	10-100 μm^2/s
D_s^j	Surface bound diffusion	0-12 μm^2/s
Q	Flow Rate	10-100 μL/min
L_w	Width of flow chamber	3.0 mm
L	Length of flow chamber	0.7 mm
h	Height of flow chamber	100 μm

C. Ion Channel-Switch Biosensor: Streptavidin, TSH, Ferritin, hCG Experimental Results

In this section the model developed in Section III-B, which relates membrane conductance to analyte concentration, is applied to experimental measurements of: streptavidin, thyroid stimulating hormone (TSH), ferritin, and human chorionic gonadotropin (hCG). As shown, the numerically predicted impedance from the reaction-diffusion model coupled with fluid flow dynamics provide accurate predictions of the biosensor response over a wide range of analyte concentrations.

Fig. 5 presents the experimentally measured and numerically predicted conductance of the ICS biosensor for the concentration estimation of streptavidin, TSH, and ferritin. As seen, the experimentally measured conductance is in good agreement with the numerically predicted conductance. For low analyte concentrations (i.e., pM), the diffusive dynamics of the analyte significantly influences the population of gA dimers present in the tethered membrane. As seen in Fig. 5, the dynamic model

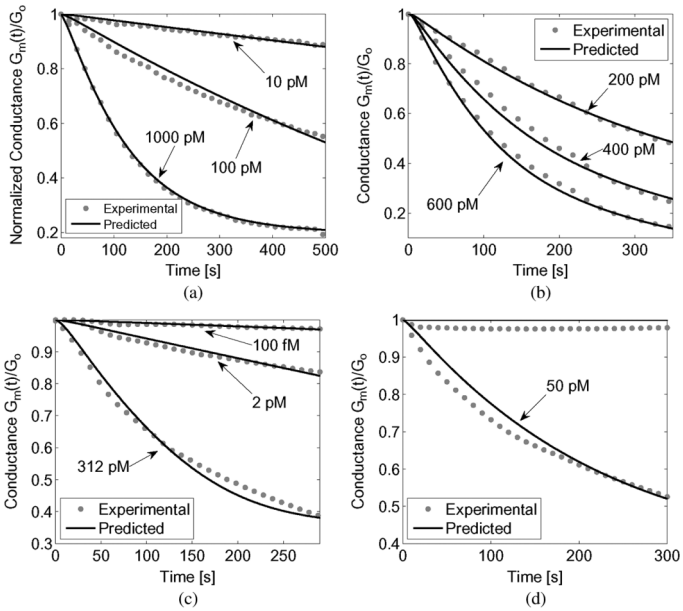

Fig. 5. Experimentally measured and numerically predicted normalized conductance $G_m(t)/G_o$ for Streptavidin, TSH and Ferritin. The numerical predictions are computed using the ICS biosensor model in Section III-B with the parameters defined in Table I. (a) Streptividin concentrations c_A: 10 pM, 100 pM, 1000 pM. (b) Ferritin in PBS, concentrations c_A: 200 pM, 400 pM, 600 pM. (c) TSH concentrations c^A: 312 pM, 2 pM, 100 fM. (d) Ferritin in whole blood, concentrations c^A: 0 pM, 50 pM.

presented in Section III-B can account for the diffusive dynamics. This allows the dynamic model to be used for not only concentration estimation, but the design of the ICS biosensor. If a specific concentration of analyte is to be measured using the ICS biosensor, the dynamic model presented in Section III-B can be used to select the number of binding sites and flow rate necessary for measurement. This procedure was applied for the design of the number of binding sites for the detection of TSH from 100 fM–350 pM, and for the detection of ferritin from 100 fM-100 pM. As seen in Fig. 5(c), using the selected number of binding sites, mobile gA monomers, and flow rate, the concentration of TSH in the range of 100 fM–350 pM can be estimated using the ICS. Fig. 5(d) presents the measurement of ferritin in whole blood. As mentioned in Section I, the ICS is designed to only detect specific target species. As thousands of molecular compounds are present in human blood, a remarkably good estimate of ferritin can be obtained using the measured impedance of the ICS and the predictive model presented in Section III-B.

Fig. 6 presents the measured and numerically predicted conductance of the ICS biosensor for the concentration estimation of hCG. For concentrations of hCG above 10 nM in blood or urine, this suggests a blastocyst or mammalian embryogenesis is present. The experimentally measured concentrations of hCG used are 0 nM and 353 nM. As seen from Fig. 6, these produce very different membrane conductance dynamics. This could alone be used as a test for pregnancy; however, it is of clinical importance to know the concentration of hCG present. Using the experimentally measured impedance and the predictive model in Section III-B, an accurate estimate of the concentration of hCG is possible. From Fig. 6, at $t = 40$ seconds,

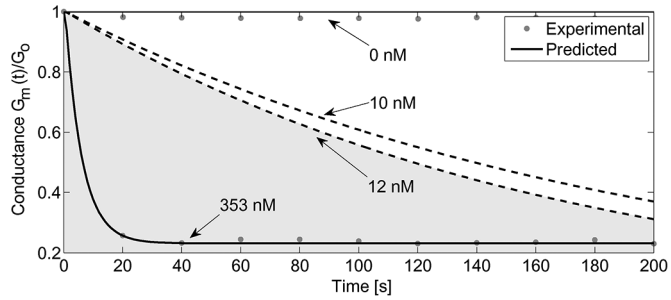

Fig. 6. Experimentally measured and numerically predicted normalized conductance $G_m(t)/G_o$ for the human chorionic gonadotropin (hCG) concentrations c^A: 0 nM, 353 nM. The numerical predictions are computed using the ICS biosensor model in Section III-B with the parameters defined in Table I.

the change in the number of conducting gA dimers is negligible. Therefore the membrane conductance is at its equilibrium value and results because only aqueous pores are present for $t > 40$ s.

In [10], clinical samples were used to establish that the ICS biosensor can detect influenza A. In a clinical environment, it is of importance to estimate the concentration of airborne influenza A. Using the models presented in this paper, the ICS biosensor can be designed for this purpose.

IV. Measurement Platform 3: Electroporation Measurement Platform (EMP)

In this section the dynamic model and experimental measurements of the EMP are presented. Using the experimental measurements from the EMP and the dynamic model allow biologically important parameters such as the characteristic voltage of electroporation and equilibrium pore density to be estimated. Since the lipid composition of the EMP can be adjusted, this allows the EMP and dynamic model to be used for the design of novel electrochemotherapy protocols. The EMP is formed using an identical procedure as presented for the PFMP in Section II-A.

A. Electroporation Measurement Platform: Dynamic Model

In this section a dynamic model of the EMP is derived for use in the estimation of important electroporation parameters. The dynamic model is constructing using asymptotic approximations to the Smoluchowski-Einstein equation for electroporation, and the GPNP presented in Section III-B.

Dynamics of Pore Radii and Population: The process of electroporation involves the nucleation and destruction of aqueous pores in response to a sufficiently high (i.e., above 50 mV) transmembrane potential. The population and dynamics of pore radii cause the membrane conductance, denoted by G_m, to change. The dynamics of the membrane conductance can be linked to the population and dynamics of the pore radii using

$$\begin{aligned} G_m &= \sum_{i=1}^{\lfloor N(t) \rfloor} G_p(r_i), \\ \frac{dr_i}{dt} &= -\frac{D}{k_B T}\frac{\partial W(r, V_m)}{\partial r_i} \quad \text{for} \quad r_i \in \{1, 2, \ldots, \lfloor N(t) \rfloor\}, \\ \frac{dN}{dt} &= \alpha e^{\left(\frac{V_m}{V_{ep}}\right)^2}\left(1 - \frac{N}{N_o}e^{-q\left(\frac{V_m}{V_{ep}}\right)^2}\right). \end{aligned} \tag{9}$$

In (9), D is the radial diffusion coefficient of pores, k_B is Boltzmann constant, T is the temperature, α is the pore creation rate coefficient, V_{ep} is the characteristic voltage of electroporation, N is the number of pores, $N_o = G_o/G_p(r_m)$ is the pore density at $V_m = 0$, and $q = (r_m/r_*)^2$ is the squared ratio of the minimum energy radius r_m at $V_m = 0$ with r_* the minimum energy radius of hydrophilic pores [30]–[33]. The initial conditions of (9) are that $N(0) = N_o$ and all created pores r_i initially start with a radius of r_m. The values of the parameters in (9) are specified in Table III.

The derivation of (9) is based on making physiologically relevant approximations to the Smoluchowski-Einstein equation for electroporation. The Smoluchowski-Einstein equation governs the distribution of pores as a function of their radius r and time t [14]–[16]. If we denote $n(r,t)$ as the pore density distribution function, then the Smoluchowski-Einstein equation is given by

$$\frac{\partial n}{\partial t} = D\frac{\partial}{\partial r}\left[\frac{n}{k_B T}\frac{\partial W}{\partial r} + \frac{\partial n}{\partial r}\right] + S(r) \tag{10}$$

where D is the diffusion coefficient of pores, k_B is the Boltzmann constant, T is the temperature, W is the pore energy, and $S(r)$ models the creation and destruction rate of pores. Typical initial and boundary conditions for (10) can be found in [14], [19], [20], [34]. Aqueous pore formation involves the creation of a hydrophilic pore, generally assumed to by a water filled cylinder with a free energy given in terms of modified Bessel's functions, which either spontaneously convert to a stable hydrophobic pore or spontaneously collapse [20], [35], [36]. The parameter $S(r)$ accounts for the hydrophilic to hydrophobic energy transition. Detailed discussion of the transition from hydrophilic to hydrophobic pore structure is provided in [14]–[16], [19], [34]. Making the physiologically relevant assumption that the diffusion term in (10) (i.e., $\partial n/\partial r$) is negligible, and the characteristic time scale of W is longer then 0.1 μs, the process of electroporation can be modelled by (9).

GPNP for Electroporation Measurement Platform: To compute the ionic flux J^i and electrical potential ϕ necessary for evaluating the pore conductance G_p and electrical energy required to form a pore $W_{\rm es}$, the GPNP model (3) is used. Here the necessary boundary and initial conditions for computing J^i and ϕ are defined.

Although different pore shapes and corresponding pore energies can be considered for the hydrophobic pore, typically a toroidal pore is assumed [18], [19], [37]. Note that the toroidal structure corresponds to the estimated hydrophobic pore shape obtained from molecular dynamics simulations [38], [39]. In this paper we consider the toroidal pore structure illustrated in Fig. 7 to compute J^i and ϕ for evaluating J^i and ϕ. The material and boundary conditions of (3) for computing J^i and electric field ϕ are given by

$$n \cdot J^i = 0 \text{ in } \partial\Omega_m \cup \partial\Omega_e \cup \partial\Omega_{ec}, \tag{11a}$$

$$a\phi_m - \phi_w = 0 \text{ in } \partial\Omega_m,$$

$$\varepsilon_m \nabla\phi_m \cdot n - \varepsilon_w \nabla\phi_w \cdot n = 0 \text{ in } \partial\Omega_m, \tag{11b}$$

$$C_s(\phi_e - \phi) + \varepsilon_w n \cdot \nabla\phi = 0 \text{ in } \partial\Omega_e,$$

$$C_s(\phi_{ec} - \phi) + \varepsilon_w n \cdot \nabla\phi = 0 \text{ in } \partial\Omega_{ec}, \tag{11c}$$

$$c^i = c_o^i \text{ in } \partial\Omega_w,$$

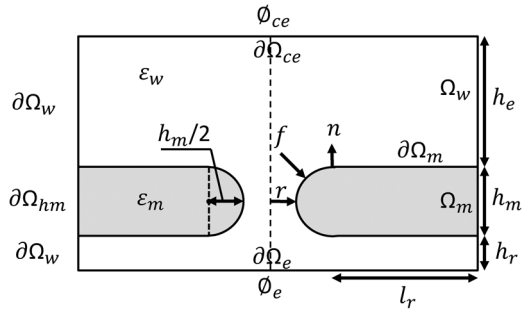

Fig. 7. Geometry and boundary conditions for (3), denoted by $\partial\cdot$, for estimating G_p and $W_{\rm es}$. The aqueous pore is modelled as axisymmetric with dimensions given by r, l_r, h_r, h_m, and h_e. The potentials at each electrode are defined by ϕ_e and ϕ_{ec} respectively. The electrolyte has an electrical permittivity ε_w and the membrane an electrical permittivity ε_m.

$$n \cdot \nabla\phi = 0 \text{ in } \partial\Omega_{hm} \cup \partial\Omega_w \tag{11d}$$

Eq. (11a) states that the membrane surface is assumed to be perfectly polarizable (i.e., blocking) such that the normal ionic flux vanishes at the surface of the membrane. There are no surface reactions present at the bioelectronic interface; therefore, a no-flux boundary condition is present at the gold surface. To ensure the well-posedness of the Poisson (3b), the internal boundary conditions on the membrane to electrolyte interface are satisfied by (11b) [40]. At the electrode surface a compact Stern layer exists with a capacitance per unit are given by C_s. The Stern layer adjacent to the electrodes is modelled using (11c) with ϕ_e and ϕ_{ec} the prescribed potentials at the respective electrodes. Eq. (11d) provides the ambient boundary conditions away from the pore with c_o^i the initial concentration.

Pore Conductance and Electrical Energy: In this section the pore conductance G_p and electrical energy required to form a pore $W_{\rm es}$ are evaluated using the computed J^i and ϕ from the GPNP (3) with boundary conditions (11). The conductance of the pore G_p is evaluated using

$$I_p = F\sum_i \int_0^r J^i(r) 2\pi\, r dr, \quad G_p = \frac{I_p}{V_m} \tag{12}$$

where J^i is the flux of species i, r is the radius of the pore, V_m is the transmembrane potential, and F is the Faraday constant. To evaluate $W_{\rm es}$, assuming negligible osmotic pressure, local mechanical equilibrium, and that pore expansion is isolated to the radial direction, the following is used [18], [41], [42]

$$\begin{aligned} W_{\rm es}(r) &= -\int_0^r \left(\int_S n \cdot (T_w - T_m) n dS\right) dr, \\ T_w &= \varepsilon_w \left(\frac{1}{2}|\nabla\phi_w|^2 I - \nabla\phi_w \otimes \nabla\phi_w\right), \\ T_m &= \varepsilon_m \left(\frac{1}{2}|\nabla\phi_m|^2 I - \nabla\phi_m \otimes \nabla\phi_m\right). \end{aligned} \tag{13}$$

In (13), T_w and T_m are the Maxwell stress tensors [18], [42], I denotes the identity matrix, n denotes the normal vector (Fig. 7), S the surface of the pore, and $\otimes$ is the dyadic product (i.e., $\nabla\phi \otimes \nabla\phi = \nabla\phi\nabla\phi^T$). The expression $f = (T_w - T_m)n$ denotes the electrical force density on the surface of the pore.

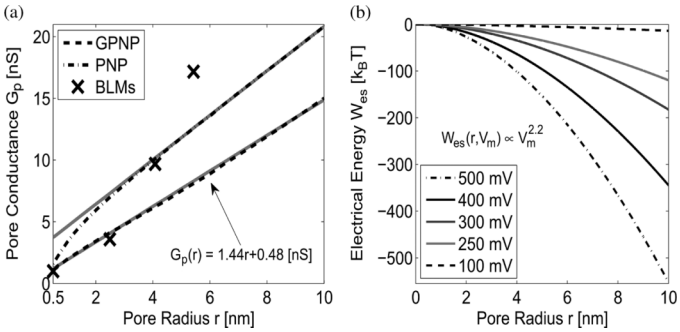

Fig. 8. Numerically predicted G_p (12) and $W_{\rm es}$ (13) computed using the GPNP model in Section IV-A with parameters defined in Table II. The experimentally measured conductance (BLMs) is obtained from [43]–[45].

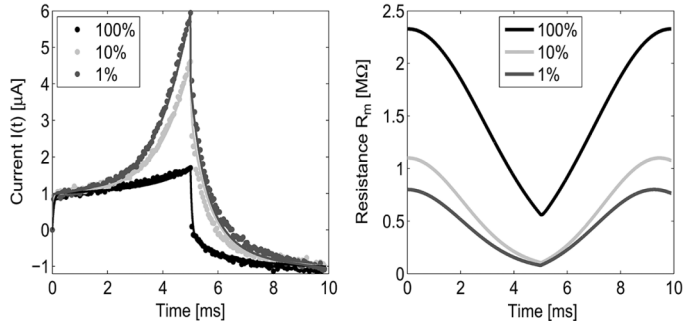

Fig. 9. Experimentally measured and numerically predicted current $I(t)$, and membrane resistance $R_m = 1/G_m$, for tethered DphPC membranes resulting from a triangular drive potential $V_s(t)$ at a rate of 100 V/s for 5 ms. All predictions are computed using the model specified by (2) and (9) with the parameters defined in Table III.

The pore conductance G_p (12) and electrical energy required to form a pore $W_{\rm es}$ (13) are evaluated using J^i and ϕ computed from (3) with boundary conditions (11).

B. Electroporation Measurement Platform: Experimental Results

In this section the experimentally measured and numerically predicted current response of the EMP are compared to validate the accuracy of the dynamic models presented in Section IV-A. Model validation is performed for different tether densities, excitation potentials, and membrane compositions. To ensure only the process of electroporation is present the following test is performed for all experimental measurements. An excitation potential V_s is applied and the resulting current is recorded, then $-V_s$ is applied and the resulting current recorded. If the current response resulting from V_s is related to the current response of $-V_s$ by a sign change then only the process of electroporation is present. This result follows from the dynamic model of the EMP given by (2) and (9). All experimental measurements satisfied this test.

Fig. 8 presents the numerically computed pore conductance G_p (12) and electrical energy required to form a pore $W_{\rm es}$ (13) evaluated using the GPNP model in Section IV-A. In Fig. 8(a) the estimated pore conductance computed using the GPNP, and PNP models is presented. As seen, the computed conductance is in agreement with the experimentally measured conductance of a single pore obtained from planar bilayer membranes (BLMs) using patch-clamp and linearly rising current protocols [43]–[45]. As expected, for pore radii $r > 3$ nm the experimentally measured conductance from the BLMs is larger then for the EMP as the electrode surface in the BLMs is not in close proximity (i.e., 4 nm) to the membrane surface in the BLM experimental setup [43]–[45]. In Fig. 8(a), the GPNP and PNP models produce differing conductance estimates as a result of the steric effects present. Recall, from Section III-B, that for $\sum_{j=1}^{N} N\mathrm{A}a_j^3 c^j \ll 1$ the steric effects are negligible and the estimated conductance using the GPNP and PNP models would be identical. From Fig. 8(a), the computed conductance approximately follows a $G_p \propto r$ relationship. A surprising result at first glance, however if we consider the literature on "spreading conductance" [15], [21], [46], [47], it must be the case that the spreading conductance caused in the $h_r = 4$ nm tethering reservoir above the bioelectronic interface dominates the pore conductance. Fig. 8(b) presents the numerically computed $W_{\rm es}$ using the GPNP defined in Section IV-A. The results compare favourably with previously computed $W_{\rm es}(r, V_m)$ using simplified governing equations that do not include electrodiffusive effects [18], [35]. From Fig. 8(b), the proportionality between $W_{\rm es}$ and V_m follows a fractional power law. Typically the assumption of a squared law is used to compute $W_{\rm es}$ [18], [35]. This assumption is valid for narrow cylindrical pores where $\partial\phi/\partial r \approx 0$ and $\partial\phi/\partial z \approx V_m/h_m$ on the surface of the pore. The computed ϕ using the GPNP does not satisfy these conditions on the pore surface illustrating the importance of including the electrodiffusive dynamics of the electrolyte.

Fig. 9 presents the experimentally measured and numerically predicted current response of the EMP for the 1% and 10% DphPC bilayer, and the 100% DphPC monolayer tethered membranes. As expected, the effects electroporation decrease as the tether density increases—that is, the tethers provide structural support hindering the nucleation of pores reducing the equilibrium pore density N_o and increasing the characteristic voltage of electroporation V_{ep}. As seen in Fig. 9, the resistance begins to change at $t \approx 1$ ms when the transmembrane potential is sufficiently high to cause the nucleation of pores. For the 100% tethered membrane, pore expansion is hindered by the tethers, therefore changes in resistance are primarily a result of pore nucleation and destruction governed by (9). For the 100% tethered membrane, it may be the case that all pores in the membrane are hydrophilic as the tethers may prevent the transition from the hydrophilic to hydrophobic structure. If only hydrophilic pores are present, the membrane resistance is dominated by the nucleation of pores and not the dynamics of the pores. Note that the molecular structure of the aqueous pores can not be reliably inferred using continuum theory models and would require the use of molecular dynamics or similar non-continuum models. Interestingly, for the 1% membrane structures the resistance begins to decrease at 9.2 ms, and for the 10% membrane at 9.4 ms after the initial application of the drive potential $V_s(t)$ defined at the beginning of this section. This is a result of the charge accumulation in the electrical double layers at the gold electrode surface, V_{dl}, discharging causing an increase in the magnitude of the transmembrane potential V_m. This illustrates the importance of

TABLE II
PARAMETER FOR G_p AND $W_{\rm es}$ PREDICTIONS

Symbol	Definition	Value
$c^{\rm Na}\|_{t=0}$	Initial Na+ concentration	321.45 mol/m^3
$c^{\rm K}\|_{t=0}$	Initial K+ concentration	13.39 mol/m^3
$c^{\rm Cl}\|_{t=0}$	Initial Cl− concentration	334.84 mol/m^3
$a_{\rm Na}$	Na+ effective ion size	4 Å
$a_{\rm K}$	K+ effective ion size	5 Å
$a_{\rm Cl}$	Cl− effective ion size	4 Å
$D_w^{\rm Na}$	Na+ diffusion coefficient in Ω_w	1.33×10^{-9} m^2/s
$D_w^{\rm K}$	K+ diffusion coefficient in Ω_w	1.96×10^{-9} m^2/s
$D_w^{\rm Cl}$	Cl− diffusion coefficient in Ω_w	2.07×10^{-9} m^2/s
ε_w	Electrolyte electrical permittivity	7.083×10^{-10} F/m
ε_m	Membrane electrical permittivity	1.771×10^{-11} F/m
F	Faraday constant	9.6485×10^4 C/mol
C_s	Stern layer capacitance	1 pF
k_B	Boltzmann constant	$1.3806488 \times 10^{-23}$ J/K
T	Temperature	300 K
ϕ_e	Electrode potential	100-500 mV
ϕ_{ec}	Counter electrode potential	0 mV
l_r	Tether reservoir length	400 nm
h_r	Tether reservoir height	4 nm
h_m	Membrane thickness	4 nm
h_e	Electrolyte height	60 nm

TABLE III
PARAMETERS FOR EMP CURRENT PREDICTIONS

Symbol	Definition	Value		
γ	Edge energy	1.8×10^{-11} J/m		
σ	Surface tension	1×10^{-3} J/m^2		
α	Creation rate coefficient	1×10^{9} s^{-1}		
q	$q=(r_m/r_*)^2$	2.46		
C	Steric repulsion constant	9.67×10^{-15} J$^{1/4}$ m		
D	Radial diffusion coefficient	1×10^{-14} m^2/s		
r_m	Equilibrium pore radius	0.8 nm		
$G_p(r_m)$	Equilibrium pore conductance	1.56 nS		
R_e	Electrolyte resistance	3.0-6.0 kΩ		
DphPC Membrane	**Tether Density:**	**1%**	**10%**	**100%**
G_0	Initial membrane conductance	1.00-1.67 μS	0.91-1.00 μS	0.43 μS
C_m	Membrane capacitance	10.5-14.6 nF	10.5-16.0 nF	11.0 nF
C_{dl}	Double-layer capacitance	39-136.3 nF	65-136.3 nF	118.2 nF
V_{ep}	Voltage of electroporation	360-430 mV	370-430 mV	580 mV
K_t	Spring constant	0 N/m	0 N/m	20 mN/m
S. cerevisiae Membrane	**Tether Density:**	**1%**	**10%**	
G_0	Initial membrane conductance	4.35 μS	2.22 μS	
C_m	Membrane capacitance	11.0 nF	9.5 nF	
C_{dl}	Double-layer capacitance	109.1 nF	136.6 nF	
V_{ep}	Voltage of electroporation	330 mV	485 mV	
K_t	Spring constant	0 N/m	0 N/m	
E. coli Membrane	**Tether Density:**	**1%**	**10%**	
G_0	Initial membrane conductance	1.81 μS	1.61 μS	
C_m	Membrane capacitance	8.8 nF	7.8 nF	
C_{dl}	Double-layer capacitance	136.6 nF	136.6 nF	
V_{ep}	Voltage of electroporation	400 mV	420 mV	
K_t	Spring constant	0 N/m	0 N/m	

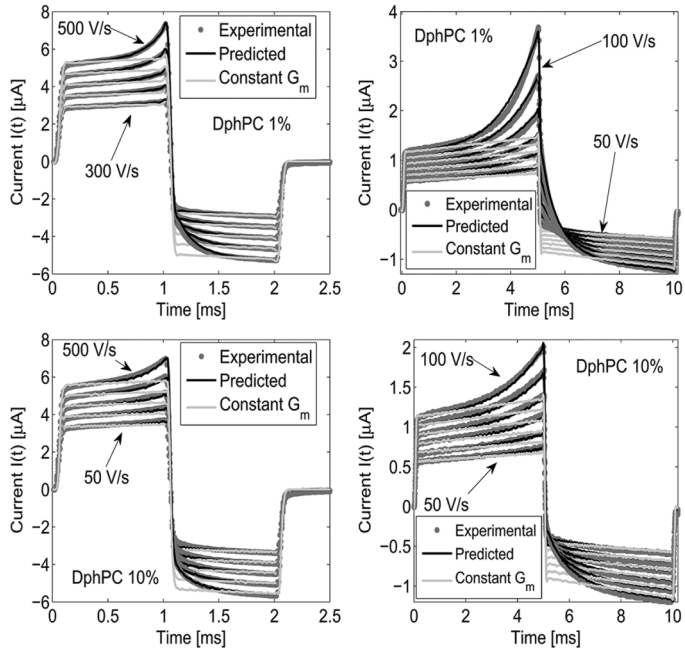

Fig. 10. Experimentally measured and numerically predicted current response $I(t)$ for the 10% and 1% tethered DphPC membrane. The triangular drive potential V_s is defined by a 300–500 V/s for 2 ms, and 50–100 V/s for 5 ms. All predictions are computed using (2) and (9) with the parameters defined in Table III.

including electrical double-layer effects when modelling gold electrodes. The thickness of the membrane can be estimated using $h_m = \varepsilon_m A_m / C_m$ with $A_m = 1.2$ mm^2, the area of the membrane surface, and ε_m and C_m given in Tables II and III. For the 1%, 10%, and 100% membranes we obtain a thickness of: 3.54 nm, 3.54 nm, 3.40 nm. These values are in excellent agreement with neutron reflectometry measurements of similar DphPC based tethered membranes [2]. As seen, the thickness of the tethered DphPC membrane is approximately constant between the 1% and 10% tether densities. The 100% DphPC monolayer is slightly thinner then the 1% and 10% DphPC bilayer membrane. This is a result of the combined effect of an increased tether density and the dibenzyl group that binds the phytanyl tails in the tethered DphPC monolayer.

In Fig. 10 the experimentally measured and numerically predicted current $I(t)$ is provided for several different linearly increasing and decreasing drive potentials. As seen from Fig. 10, excellent agreement between the experimentally measured and numerically predicted current is obtained. For small magnitude drive potentials one would expect the membrane resistance to remain constant as the effects of electroporation, governed by (2) and (9), are negligible. Indeed this is the case as electroporation is only present in the 1 ms drive for potentials above 300 V/s, and 5 ms for potentials above 50 V/s. The reason the 5 ms rise, refer to Fig. 10, has larger relative electroporation effects as compared with the 1 ms rise is that the nucleation and dynamics of pore radii evolve for a longer period of time. As expected, the magnitude of the current response for the 10% tethered membrane is less than the current response for the 10% tethered membrane as a result of the tethers hindering the nucleation and expansion of pores. The estimated electrical double-layer capacitance used to compute the current for the 10% membrane is $C_{dl} = 65$ nF, and that for the 1% tether density is $C_{dl} = 39$ nF. In reference to Table III, the expected value of C_{dl} in the range of 118–137 nF. Despite this minor discrepancy, the estimated current, using the model given in (2) and (9), is in excellent agreement with the experimentally measured current.

Fig. 11 presents the experimentally measured and numerically predicted current response of the 1% and 10% tether density DphPC, a mixed *Saccharomyces cerevisiae* lipid, and a mixed *Escherichia coli* lipid membranes. DphDC lipids with specialized moieties (i.e., methyl group in the tails, ether

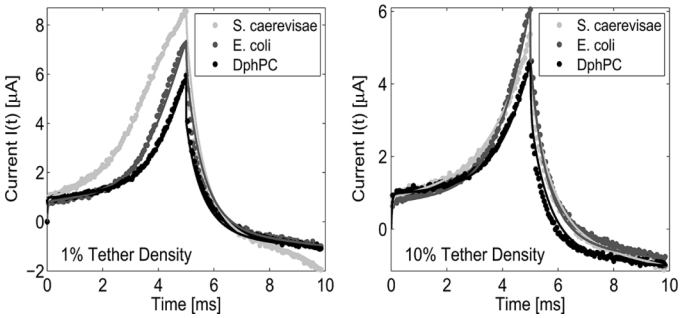

Fig. 11. Experimentally measured and numerically predicted current $I(t)$ for the 1% and 10% tethered DphPC, S. caerevisae, and E. coli membranes for a triangular drive potential $V_s(t)$ at a rate of 100 V/s for 5 ms. All predictions are computed using (2) and (9) with the parameters defined in Table III.

linkers connecting the head group and hydrophobic tail, and the phytanyl group in the tail) are expected to have a high resistivity against the effects of electroporation when compared with the mixed lipid E. coli and S. caerevisae membranes [48]. Indeed from Fig. 11 we see that the tethered DphPC membrane has a higher resistance to the effects of electroporation when compared with that of E. coli and S. caerevisae membranes. In reference to Fig. 11, the increase in tether density causes a decrease in current, this is expected because the tethers increase the stability of the membrane. The thickness of the mixed lipid E. coli membrane for the 1% and 10% tether density is 4.20 nm and 4.78 nm respectively, as compared with the mixed lipid S. caerevisae membrane with thickness 3.68 nm and 3.98 nm respectively. Indeed for the 1% tether density the effects of electroporation are more pronounced for the S. caerevisae membrane compared to the E. coli membrane as seen in Fig. 11. For the 10% tether density, the E. coli and S. caerevisae membrane thickness increases when compared with the thickness for the 1% tether density. Remarkably, from Fig. 11, the effects of electroporation are more pronounced for the E. coli then for the S. caerevisae membrane. This occurs because the increase in tether density has the effect of decreasing the probability of pore nucleation in the S. caerevisae membrane when compared to the E. coli membrane. Note that to gain insight into why the increase in tether density causes the S. caerevisae membrane to become more resilient to electroporation compared to that of the E. coli membrane requires sophisticated models such as molecular dynamics.

V. Conclusion

This paper has presented the construction, dynamic models, and experimental validation of three engineered tethered membrane based measurement platforms, namely PFMP, ICS and EMP. In all three platforms, modelling the dynamics of the bioelectronic interface and membrane conductance is of central importance for measurement. Using a lumped circuit model to account for the bioelectronic interface, we provided experimental results illustrating how the PFMP can be used to measure the pore forming dynamics of PGLa and α-Hemolysin and which type of membranes are susceptible to pore formation. Using an advection-diffusion PDE coupled with nonlinear surface reaction-diffusion PDEs, we illustrated how the measured membrane conductance of the ICS can be used to detect pico-molar concentrations of streptavidin, ferritin, thyroid stimulating hormone, and human chorionic gonadotropin. Using specific molecular receptors, the ICS can be designed to detect viruses and bacterial molecules of interest for rapid on-site diagnosis. We developed a model for computing the conductance and electrical energy required to form a pore that includes Stern and diffuse layer effects. These were coupled with asymptotic approximations to the Smoluchowski-Einstein equation to predict the current response of the EMP, which compared favourably with experimental measurements.

Appendix
Parameters for Predictive Models

All PDEs were solved using the commercially available finite element solver COMSOL Multiphysics 4.3a, and all ODEs were solved using the MATLAB function ode15s. For (9), the numerical algorithm presented in [30], [31] was implemented. All experimental measurements, unless otherwise stated, were conducted at 20°C in a phosphate buffered solution (PBS) with a pH of 7.2, and a 0.15 M saline solution composed of Na^+, K^+, and Cl^-. At this temperature the tethered membrane is in the liquid phase. A pH of 7.2 was selected to match that typically found in the cellular cytosol of real cells.

The forward and reverse reaction rates in Table I are obtained from [9]–[11]. All other parameters are defined by the experimental setup of the ICS biosensor. In Table II, the concentrations match those used in the experimental measurements of the EMP. The selection of effective ion size (i.e., solvated ionic radius) is based on the mobility measurements reported in [49]. The diffusion coefficients of the ions and electrical permittivities of water and biological membrane are provided in [50]. The geometric parameters h_r and h_m are selected to match the experimentally measured results obtained from neutron-reflectometry measurements of similar tethered membranes reported in [2]. The parameters G_o, C_m, C_{dl}, and R_e in Table III are estimated using a single impedance measurement for each tethered membrane. The electroporation parameters $\gamma, \sigma, C, D, r_m$ are obtained from [16], [19], [30], [31], [36]. Since α and q are not dependent on the tether density, only a single current measurement was used to estimate these parameters, and found to be consistent with those reported in [36].

References

[1] W. Hoiles, V. Krishnamurthy, C. Cranfield, and B. Cornell, "An engineered membrane to measure electroporation: Effect of tethers and bioelectronic interface," *Biophys. J.*, vol. 107, no. 6, pp. 1467–1488, 2014.

[2] F. Heinrich, T. Ng, D. Vanderah, P. Shekhar, M. Mihailescu, H. Nanda, and M. Losche, "A new lipid anchor for sparsely tethered bilayer lipid membranes," *Langmuir*, vol. 25, no. 7, pp. 4219–4229, 2009.

[3] D. McGillivray, G. Valincius, D. Vanderah, W. Febo-Ayala, J. Woodward, F. Heinrich, J. Kasianowicz, and M. Lscheb, "Molecular-scale structural and functional characterization of sparsely tethered bilayer lipid membranes," *Biointerphases*, vol. 2, no. 1, pp. 21–33, 2007.

[4] B. Cornell, V. Braach-Maksvytis, L. King, P. Osman, B. Raguse, L. Wieczorek, and R. Pace, "A biosensor that uses ion-channel switches," *Nature*, vol. 387, no. 1, pp. 580–583, 1997.

[5] B. Raguse, V. Braach-Maksvytis, B. Cornell, L. King, P. Osman, R. Pace, and L. Wieczorek, "Tethered lipid bilayer membranes: Formation and ionic reservoir characterization," *Langmuir*, vol. 14, no. 3, pp. 648–659, 1998.

[6] J. Prashar, P. Sharp, M. Scarffe, and B. Cornell, "Making lipid membranes even tougher," *J. Mater. Res.*, vol. 22, pp. 2189–2194, 2007.

[7] I. Vockenroth, P. Atanasova, A. Jenkins, and I. Kper, "Incorporation of α-Hemolysin in different tethered bilayer lipid membrane architectures," *Langmuir*, vol. 24, no. 2, pp. 496–502, 2008.
[8] D. McGillivray, G. Valincius, F. Heinrich, J. Robertson, D. Vanderah, W. Febo-Ayala, I. Ignatjev, M. Lsche, and J. Kasianowicz, "Structure of functional staphylococcus aureus α-Hemolysin channels in tethered bilayer lipid membranes," *Biophys. J.*, vol. 96, no. 4, pp. 1547–1553, 2009.
[9] S. Moradi-Monfared, V. Krishnamurthy, and B. Cornell, "A molecular machine biosensor: Construction, predictive models and experimental studies," *Biosens. Bioelectron.*, vol. 34, no. 1, pp. 261–266, 2012.
[10] V. Krishnamurthy, S. Monfared, and B. Cornell, "Ion-channel biosensors part I: Construction, operation, clinical studies," *IEEE Trans. Nanotechnol.*, vol. 9, no. 3, pp. 303–312, 2010.
[11] V. Krishnamurthy, S. Monfared, and B. Cornell, "Ion channel biosensors Part II: Dynamic modeling, analysis, statistical signal processing," *IEEE Trans. Nanotechnol.*, vol. 9, no. 3, pp. 313–321, 2010.
[12] G. Woodhouse, L. King, L. Wieczorek, and B. Cornell, "Kinetics of the competitive response of receptors immobilised to ion-channels which have been incorporated into a tethered bilayer," *Faraday Discuss.*, vol. 111, pp. 247–258, 1999.
[13] S. El-Andaloussi, Y. Lee, S. Lakhal-Littleton, J. Li, Y. Seow, C. Gardiner, L. Alvarez-Erviti, I. Sargent, and M. Wood, "Exosome-mediated delivery of sirna *in vitro* and *in vivo*," *Nature Protocols*, vol. 7, no. 12, pp. 2112–2126, 2012.
[14] V. Pastushenko, Y. Chizmadzhev, and V. Arakelyan, "Electric breakdown of bilayer lipid membranes: II. Calculation of the membrane lifetime in the steady-state diffusion approximation," *J. Electroanal. Chem. Interfacial Electrochem.*, vol. 104, no. 0, pp. 53–62, 1979.
[15] A. Barnett and J. Weaver, "Electroporation: A unified, quantitative theory of reversible electrical breakdown and mechanical rupture in artificial planar bilayer membranes," *Bioelectrochem. Bioenerget.*, vol. 25, no. 2, pp. 163–182, 1991.
[16] S. Freeman, M. Wang, and J. Weaver, "Theory of electroporation of planar bilayer membranes: Predictions of the aqueous area, change in capacitance, pore-pore separation," *Biophys. J.*, vol. 67, no. 1, pp. 42–56, 1994.
[17] S. Talele, P. Gaynor, M. Cree, and J. Ekeran, "Modelling single cell electroporation with bipolar pulse parameters and dynamic pore radii," *J. Electrostat.*, vol. 68, no. 3, pp. 261–274, 2010.
[18] J. Neu, K. Smith, and W. Krassowska, "Electrical energy required to form large conducting pores," *Bioelectrochem.*, vol. 60, no. 1, pp. 107–114, 2003.
[19] J. Neu and W. Krassowska, "Asymptotic model of electroporation," *Phys. Rev. E*, vol. 59, pp. 3471–3482, 1999.
[20] J. Neu and W. Krassowska, "Modeling postshock evolution of large electropores," *Phys. Rev. E*, vol. 67, p. 021915, 2003.
[21] J. Li and H. Lin, "The current-voltage relation for electropores with conductivity gradients," *Biomicrofluid.*, vol. 4, no. 1, 2010.
[22] M. Vela, H. Martin, C. Vericat, G. Andreasen, A. Hernandez Creus, and R. C. Salvarezza, "Electrodesorption kinetics and molecular interactions in well-ordered thiol adlayers on Au(111)," *J. Phys. Chem. B*, vol. 104, no. 50, pp. 11878–11882, 2000.
[23] G. Valincius, T. Meskauskas, and F. Ivanauskas, "Electrochemical impedance spectroscopy of tethered bilayer membranes," *Langmuir*, vol. 28, no. 1, pp. 977–990, 2011.
[24] G. Krishna, J. Schulte, B. Cornell, R. Pace, L. Wieczorek, and P. Osman, "Tethered bilayer membranes containing ionic reservoirs: The interfacial capacitance," *Langmuir*, vol. 17, no. 16, pp. 4858–4866, 2001.
[25] P. Yin, C. Burns, P. Osman, and B. Cornell, "A tethered bilayer sensor containing alamethicin channels and its detection of amiloride based inhibitors," *Biosens. Bioelectron.*, vol. 18, no. 4, pp. 389–397, 2003.
[26] L. Olesen, M. Bazant, and H. Bruus, "Strongly nonlinear dynamics of electrolytes in large AC voltages," *Phys. Rev. E*, vol. 82, p. 011501, 2010.
[27] J. Lpez-Garca, J. Horno, and C. Grosse, "Equilibrium properties of charged spherical colloidal particles suspended in aqueous electrolytes: Finite ion size and effective ion permittivity effects," *J. Colloid Interface Sci.*, vol. 380, no. 1, pp. 213–221, 2012.
[28] M. Kilic, M. Bazant, and A. Ajdari, "Steric effects in the dynamics of electrolytes at large applied voltages. II. modified Poisson-Nernst-Planck equations," *Phys. Rev. E*, vol. 75, no. 2, p. 021503, 2007.
[29] H. Wang, A. Thiele, and L. Pilon, "Simulations of cyclic voltammetry for electric double layers in asymmetric electrolytes: A generalized modified Poisson-Nernst-Planck model," *J. Phys. Chem. C*, vol. 117, no. 36, pp. 18 286–18 297, 2013.
[30] K. Smith, J. Neu, and W. Krassowska, "Model of creation and evolution of stable electropores for DNA delivery," *Biophys. J.*, vol. 86, no. 5, pp. 2813–2826, 2004.
[31] W. Krassowska and P. Filev, "Modeling electroporation in a single cell," *Biophys. J.*, vol. 92, no. 2, pp. 404–417, 2007.
[32] Q. Hu and R. Joshi, "Transmembrane voltage analyses in spheroidal cells in response to an intense ultrashort electrical pulse," *Phys. Rev. E*, vol. 79, p. 011901, 2009.
[33] S. Movahed and D. Li, "A theoretical study of single-cell electroporation in a microchannel," *J. Membrane Biol.*, vol. 246, pp. 151–160, 2013.
[34] J. Neu and W. Krassowska, "Singular perturbation analysis of the pore creation transient," *Phys. Rev. E*, vol. 74, p. 031917, 2006.
[35] I. Abidor, V. Arakelyan, L. Chernomordik, Y. Chizmadzhev, V. Pastushenko, and M. Tarasevich, "Electric breakdown of bilayer lipid membranes: I. The main experimental facts and their qualitative discussion," *J. Electroanal. Chem. Interfacial Electrochem.*, vol. 104, pp. 37–52, 1979.
[36] R. Glaser, S. Leikin, L. Chernomordik, V. Pastushenko, and A. Sokirko, "Reversible electrical breakdown of lipid bilayers: Formation and evolution of pores," *Biochimica et Biophysica Acta (BBA)-Biomembranes*, vol. 940, no. 2, pp. 275–287, 1988.
[37] A. Barnett, "The current-voltage relation of an aqueous pore in a lipid bilayer membrane," *Biochimica et Biophysica Acta (BBA)-Biomembranes*, vol. 1025, no. 1, pp. 10–14, 1990.
[38] M. Deminsky, A. Eletskii, A. Kniznik, A. Odinokov, V. Pentkovskii, and B. Potapkin, "Molecular dynamic simulation of transmembrane pore growth," *J. Membrane Biol.*, vol. 246, no. 11, pp. 821–831, 2013.
[39] J. Wohlert, W. Otter, O. Edholm, and W. Briels, "Free energy of a trans-membrane pore calculated from atomistic molecular dynamics simulations," *J. Chem. Phys.*, vol. 124, no. 15, p. 154905, 2006.
[40] Q. Zheng, D. Chen, and G. Wei, "Second-order Poisson-Nernst-Planck solver for ion transport," *J. Comput. Phys.*, vol. 230, no. 13, pp. 5239–5262, 2011.
[41] R. Joshi and Q. Hu, "Analysis of cell membrane permeabilization mechanics and pore shape due to ultrashort electrical pulsing," *Med. Biol. Eng. Comput.*, vol. 48, no. 9, pp. 837–844, 2010.
[42] F. Ziebert, M. Bazant, and D. Lacoste, "Effective zero-thickness model for a conductive membrane driven by an electric field," *Phys. Rev. E*, vol. 81, no. 3, p. 031912, 2010.
[43] S. Kalinowski, G. Ibron, K. Bryl, and Z. Figaszewski, "Chronopotentiometric studies of electroporation of bilayer lipid membranes," *Biochimica et Biophysica Acta (BBA)-Biomembranes*, vol. 1369, no. 2, pp. 204–212, 1998.
[44] K. Melikov, V. Frolov, A. Shcherbakov, A. Samsonov, Y. Chizmadzhev, and L. Chernomordik, "Voltage-induced nonconductive pre-pores and metastable single pores in unmodified planar lipid bilayer," *Biophys. J.*, vol. 80, no. 4, pp. 1829–1836, 2001.
[45] M. Kotulska, J. Basalyga, M. Derylo, and P. Sadowski, "Metastable pores at the onset of constant-current electroporation," *J. Membrane Biol.*, vol. 236, no. 1, pp. 37–41, 2010.
[46] M. Aguilella-Arzo, V. Aguilella, and R. Eisenberg, "Computing numerically the access resistance of a pore," *Eur. Biophys. J.*, vol. 34, no. 4, pp. 314–322, 2005.
[47] J. Newman, "Resistance for flow of current to a disk," *J. Electrochem. Soc.*, vol. 113, no. 5, pp. 501–502, 1966.
[48] A. Polak, M. Tarek, M. Tomšič, J. Valant, N. Ulrih, A. Jamnik, P. Kramar, and D. Miklavčič, "Electroporation of archaeal lipid membranes using MD simulations," *Bioelectrochem.*, 2014.
[49] J. Israelachvili, *Intermolecular and Surface Forces: Revised Third Edition*, 3rd ed. New York, NY, USA: Academic, 2011.
[50] R. Hobbie and B. Roth, *Intermediate Physics for Medicine and Biology*. New York, NY, USA: Springer, 2007.

William Hoiles received the M.A.Sc. degree from the Department of Engineering Science, Simon Fraser University, Vancouver, BC, Canada, in 2012.

Currently, he is working toward the Ph.D. degree in the Department of Electrical and Computer Engineering, University of British Columbia, Vancouver, BC, Canada. His research interests are the bioelectronic interface and social sensors.

Vikram Krishnamurthy (F'05) received the Ph.D. degree from Australian National University, Acton, ACT, Australia, in 1992.

Currently, he is a Professor and Canada Research Chair in the Department of Electrical Engineering, University of British Columbia, Vancouver, BC, Canada. His current research interests include statistical signal processing, stochastic control in social networks, and the dynamics of protein molecules.

Dr. Krishnamurthy served as Distinguished Lecturer for the IEEE Signal Processing Society and Editor-in-Chief of IEEE JOURNAL SELECTED TOPICS IN SIGNAL PROCESSING. He received an honorary doctorate from KTH (Royal Institute of Technology, Sweden) in 2013.

Bruce Cornell held a CSIRO postdoctoral fellowship at the University of London, London, U.K., from 1975–1977 and returned to Australia to a Senior Scientific post with CSIRO in the field of biophysics.

He was appointed the Director of the Cooperative Research Centre for Molecular Engineering (1992–1999) and founded the commercial consortium that became Ambri Ltd., for whom he worked as Chief Scientist (2000–2005). In 2005, he founded Surgical Diagnostics Ltd., where he is currently Director of Science and Technology. He is an elected member of the Australian Academy of Technological Sciences and Engineering, a member of a number of advisory groups to Australian universities, and an advisory to the Australian government on the medical device industry.